RSC Advances

PAPER

View Article Online
View Journal | View Issue

Check for updates

Cite this: *RSC Adv.*, 2024, **14**, 39418

The kinetics of a light irradiation enhanced room temperature NO_2 gas sensor using hybrid ZnO/ZnTe nanorod structures†

Nguyen Minh Hieu, *[a] Cao Van Phuoc, [b] Cao Viet Anh,[c] Nguyen Manh Hung,[e] Anh D. Phan, [a] Nguyen Duc Chinh,[b] Sutripto Majumder,[f] Truong Hong Cuong,[b] Hoang Gia Chuc,[a] Do Van Minh,[b] Do Quang Trung, [d] Tu Nguyen, [d] Nguyen Van Du,[d] Tran Manh Trung, [a] Pham Thanh Huy, [a] Jong-Ryul Jeong, [b] Chunjoong Kim[b] and Dojin Kim [b]

This study focuses on fabricating a hybrid structure consisting of ZnO nanorods and ZnTe nanoparticles for NO_2 gas detection, particularly exploring the impact of light irradiation at room temperature (RT). The morphology, physical characteristics, and chemical properties of the ZnO/ZnTe hybrid structure are carefully studied under diverse analytical methods such as X-ray diffraction (XRD), transmission electron microscopy (TEM), X-ray photoelectron spectroscopy (XPS), and other measurements. The ZnO/ZnTe composite displayed an improved response toward 500 ppb NO_2 under the blue light radiation effect. It demonstrated higher response (more than 2500%), response time (faster than 3000%), and recovery time (faster than 1000%) at RT compared with pure ZnO. Hence, blue light irradiation revealed a more promising sensing performance than UV irradiation's case (200% at sensitivity). The depletion theory, the oxygen vacancy, the catalytic effect of zinc telluride, and the absorption coefficient modulation of the gas sensor based on different materials explained the overall performance of the nanohybrid structured sensor.

Received 27th September 2024
Accepted 30th November 2024

DOI: 10.1039/d4ra06969b

rsc.li/rsc-advances

Open Access Article. Published on 13 December 2024. Downloaded on 2/20/2026 8:43:14 PM.
This article is licensed under a Creative Commons Attribution-NonCommercial 3.0 Unported Licence.

1. Introduction

Nitrogen oxide (NO_2) is globally listed as one of the most toxic and hazardous gases, posing a significant danger to human health and environmental safety records.[1–3] Particularly at low concentrations (~1 ppm), NO_2 has the potential to harm human lungs and induce severe respiratory diseases. Hence, there is an escalating need to develop highly efficient NO_2 gas sensors. Nano-chemo-resistive materials have garnered substantial attention due to their advantageous nano-level size, simple fabrication, reasonable cost, and dense structures.[4,5] Semiconducting metal oxides (SMOs), with abundant active sites on a vast area surface facilitating fast gas reactions and adsorption processes, are prominently featured as sensing materials in selected chemo-resistive gas sensors.[6–8] Various strategies have been explored to enhance gas detection, including elemental precursor doping,[9,10] nano heterojunction formation,[11,12] and noble metal addition.[13,14] Zinc oxide (ZnO), a widely researched n-type semiconductor securing a large band gap of ~3.37 eV, has applications in gas sensors, energy storage, and optoelectronic devices.[1,15–17] ZnO has been proven to have an impact on enhancing gas sensing properties under the effect of light irradiation.[15,18–22]

On the other hand, zinc telluride (ZnTe), a relatively new p-type semiconductor with a range direct band gap of approximately 2.1 to 2.6 eV, has demonstrated promising activation under light effects, improving the charge carrier for surface reaction and increasing surface reaction thermodynamic.[23–25] Adding p-type ZnTe can potentially create the p–n junction, leading to the depletion region modification.[26,27] Additionally, the visible light irradiation effect has been significantly introduced as a potential solution to enhance the gas sensing properties and reduce the response–recovery times of SMO materials at low temperatures.[28–32] However, there is no publication on the formation of a ZnO/ZnTe p–n heterojunction under light effects for room temperature (RT) NO_2 gas

[a]Faculty of Materials Science and Engineering, Phenikaa University, Yen Nghia, Ha Dong, Hanoi 12116, Vietnam. E-mail: hieu.nguyenminh@phenikaa-uni.edu.vn
[b]Department of Materials Science and Engineering, Chungnam National University, Daejeon, 34134, Republic of Korea
[c]Department of Electrical Engineering, Chungnam National University, Daejeon, 34134, Republic of Korea
[d]Faculty of Fundamental Sciences, Phenikaa University, Yen Nghia, Ha Dong, Hanoi 12116, Vietnam
[e]Department of Materials Science and Engineering, Le Quy Don Technical University, Hanoi 100000, Vietnam
[f]Department of Physics, School of Natural Science, Yeungnam University, Gyeongsan, 38541, Republic of Korea

† Electronic supplementary information (ESI) available. See DOI: https://doi.org/10.1039/d4ra06969b

© 2024 The Author(s). Published by the Royal Society of Chemistry

Open Access Article. Published on 13 December 2024. Downloaded on 2/20/2026 8:43:14 PM. This article is licensed under a Creative Commons Attribution-NonCommercial 3.0 Unported Licence.

detection. Motivated by the potential idea of combining the heterostructure p–n junction and the lack of relevant studies, we proposed and successfully fabricated a nanohybrid of p-ZnTe/n-ZnO nanorods with enhanced gas sensing detection at RT (25 °C) toward 500 ppb NO_2 gas under a blue (460 nm) light effect. Our studies show higher response, smaller measuring temperature, smaller irradiated light energy, and smaller gas concentration in comparison with other recent studies as shown in the discussion part. The sensor also exhibited shorter response and recovery time, high selectivity, and stability toward target gases under light illumination.

2. Experimental section

2.1 Preparation of nanohybrid ZnO/ZnTe

2.1.1. ZnO nanorod synthesis. The fabrication process is schematically drawn in Fig. 1a and was mentioned before in ref. 26. The chemical reagents of sodium tellurite (Na_2TeO_3), hexamethylenetetramine (HTMA), zinc nitrate ($Zn(NO_3)_2 \cdot 6H_2O$), and sodium borohydride ($NaBH_4$) were provided by Sigma-Aldrich. The Al_2O_3 substrates with two patterned Au electrode lines were purchased from NanoKarbon, which was deposited Zn thin film by sputtering. Thus, an oxidation treatment was pulled out at 500 °C to obtain the ZnO seed layers. The original solution for forming ZnO nanorod growth was prepared by stirring 2.4 g of $Zn(NO_3)_2 \cdot 6H_2O$ in 100 ml of deionized (DI) water with 1.12 g of HTMA in another 100 ml of DI water. The resultant formed solution was continuously stirred at RT until a transparent and clear solution appeared. The Al_2O_3 substrates with ZnO seed layers were then submerged into a reaction autoclave and subjected to hydrothermal reaction at 90 °C for 4 h. The samples collected were inserted into an oxidation treatment process at 500 °C to remove unwanted amorphous structures and to validate the crystalline ZnO nanorod.

2.1.2. ZnO/ZnTe nanohybrid synthesis. A small amount (0.05 g) of Na_2TeO_3 was put in a beaker consisting of 100 ml of DI water along with the dissolution of 0.125 g of $NaBH_4$ in another 20 ml of DI water, and both were separately controlled to be stirred continuously at 300 rpm for 15 min. Different volumes of $NaBH_4$ solution (0, 1, and 5 ml) were slowly dropped into the 100 ml Na_2TeO_3 solution to generate solutions with diverse Te concentrations. The dropping of $NaBH_4$ gradually turned the Na_2TeO_3 solution color from transparent to brown and lately to red. After that, the resulting solution was transferred again into the autoclave, and the above ZnO nanorod substrate was immersed in the autoclave, followed by the heat treatment consecutively at 95 °C for 2 h, promoting the ZnTe growth on the surface of ZnO nanorods. The ZnTe-coated ZnO nanorod structures derived from solutions with distinct Te concentrations were labeled as ZP, ZT1, and ZT5, corresponding to pristine ZnO, 1, and 5 ml dropped $NaBH_4$ solutions. The obtained samples underwent multiple rinses with DI water, were dried at 80 °C, and finally received Ar calcination at 350 °C. Consequently, a successful p-ZnTe/n-ZnO hybrid nanorod structure was collected.

2.2 Materials characterizations

The field-emission scanning electron microscopy (FE-SEM) was used to investigate the surface characteristics of the produced nanohybrid. The energy dispersive spectroscopy (EDS) equipped with SEM was deployed to examine the elemental distribution. High-resolution transmission electron microscopy (HR-TEM) was employed to analyze the structural properties of the sensing materials. X-ray diffraction (XRD), X-ray photoelectron spectroscopy (XPS), and Raman spectrometry assessed the nanohybrid's crystalline characterization.

2.3 Gas sensing property measurement system

Gas sensitivity characteristics were evaluated using a source of pico-ammeter/voltage (Keithley 6487) within a customized detecting system,[33–35] as illustrated in Fig. 1b. The analyte gas, which in this research is NO_2, was released from gas cylinders at concentrations of 1000 ppm, the diluted environment is nitrogen. The analyte gas was further diluted in dry air by

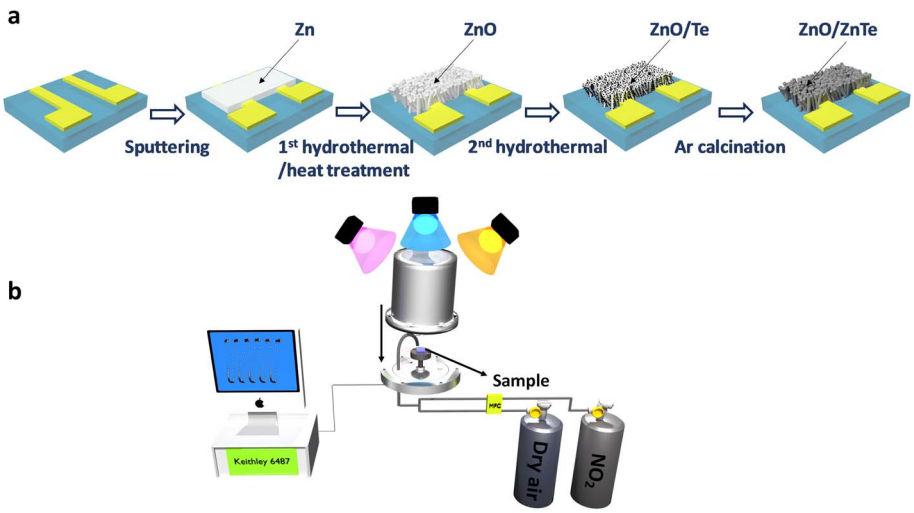

Fig. 1 (a) Fabrication process of ZnO/ZnTe nanohybrid structures and (b) schematic of the gas detection system.

Open Access Article. Published on 13 December 2024. Downloaded on 2/20/2026 8:43:14 PM.
This article is licensed under a Creative Commons Attribution-NonCommercial 3.0 Unported Licence.

adjusting the analyte gas concentration at a constant dry-air flow rate of 100 sccm upon introduction into the test chamber. Dry air was the carrier gas, and a mass-flow controller controlled the incoming gas flow rate. The conductance and resistance measurements were conducted by applying a 1 V bias between the two Au electrodes while introducing dry air (R_a) or analyte gases (R_g) into the chamber with R_a, R_g was recorded by the Keithley 6487 system. The gas sensitivity detection of the n-type doped gas sensor, such as ZnO nanorods, is expressed as $S = R_g/R_a$ for oxidizing gases like NO_2; the detailed response investigations can be found in our previous research.[33,34,36,37] To investigate the light irradiation effect on the gas detection behavior, two light-emitting source wavelengths were used: blue (460 nm) and UV (365 nm), which are Prizmatix UHP-T-DI Blue LED System at 460 nm and High Power Filtered UV 365 nm Fiber-Coupled Light Source. The fixed power intensity was set at 160 μW cm^{-2}, and the illuminating power of each light source (P) was calculated by the equation: $P = I \times 4\pi r^2$ with diversified (r) is the appropriate distance from the LED illumination source to the sensors through a quartz window outside of the chamber. The measuring temperature was set at 25 °C. To operate the humidity measurement, water molecules were pumped through a bubbler, and the flow ratio was controlled by an MFC. The relative humidity values were identified by the Testo 635 Temperature and Moisture meter.

3. Results and discussion

3.1 Structure and morphology properties

The XRD patterns for the devices are depicted in Fig. 2a. The three primary peaks at 34.36°, 47.5°, and 62.8° corresponded to the diffractions of hexagonal ZnO (JCPDS card no. 36-1451) at the significant (002), (012), and (013) planes, and confirmed the formation of pure ZnO without other unknown material existence. With ZT1, the additional peaks were identified at 25.6°, 41.8°, 51.8°, and 60.6°, attributed to the (111), (022), (222), and (004) planes, which match well with the standard diffraction database JCPDS no. 15-0746 of cubic ZnTe, respectively. The Te peak (021) predominates in the ZT5 sample, along with multiple other visible Te peaks such as (010), (101), (012), *et al.* (which was referred from the JCPDS no. 79-0736), indicating a thicker Te coating layer in ZT5. Consequently, ZT1 displayed the creation of ZnTe/ZnO composition (nanohybrid p–n heterojunction) solely, whereas ZT5 exhibited the formation of ZnO/ZnTe/Te. As illustrated in Fig. 2b, an in-depth examination of the principal diffraction peak ZnO (002) indicated an increase in the peak's FWHM with the ZnTe formation. This suggests that the creation of ZnTe *via* ion exchange adversely affected the crystallinity property of the covered ZnO nanorods. The deterioration of the zinc oxide nanorods was further corroborated by the escalating relative peak intensities for the (010), (011), (110), and (112) planes of ZnO relative to the (002) peak intensity, as depicted in Fig. 2a. The sample chemical components were firmly confirmed through the XPS study, as illustrated in Fig. 2c and d. In Fig. 2c and a binding energy comparison of Zn 2p for ZP and ZT1 samples revealed a 0.25 eV negative shift in the ZT1 peak compared with ZP, which was attributed to the formation of ZnTe. The ZT1 peak exhibited a deconvolution into two peaks, which were proposedly identified as significant peaks of ZnTe and ZnO. Fig. 2d compared the Te 3d significant peaks of ZT1 and ZT5 samples, showing distinct Te thickness values. The Te 3d significant peaks of ZT1 located at 572.91 and 583.31 eV were

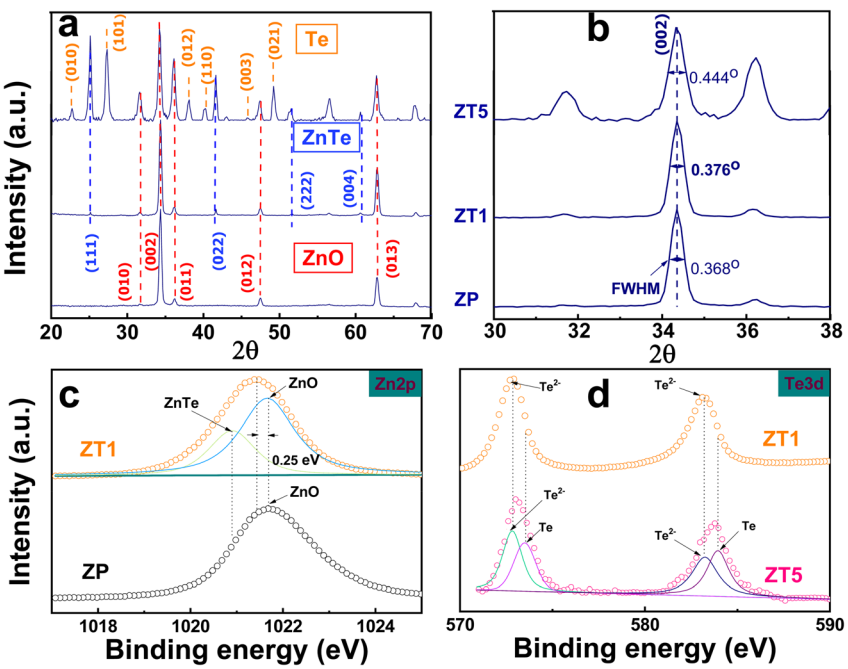

Fig. 2 (a) XRD pattern of ZP, ZT1, and ZT5. (b) The full width at half maximum (FWHM) for three samples. The XPS profiles for (c) Zn 2p of ZP compared with ZT1, and (d) Te 3d from ZT1 and ZT5.

© 2024 The Author(s). Published by the Royal Society of Chemistry

Open Access Article. Published on 13 December 2024. Downloaded on 2/20/2026 8:43:14 PM.
This article is licensed under a Creative Commons Attribution-NonCommercial 3.0 Unported Licence.

assigned correspondingly to Te^{2-} $3d_{5/2}$ and Te^{2-} $3d_{3/2}$ and confirm the existence of the ZnTe layer over the ZnO nanorod structure. Meanwhile, the Te 3d peaks of ZT_5 are separated into two peaks, one originated from ZnTe formation and the remaining one from Te metal.

Fig. 3a–c represents the scanning electron microscopy (SEM) images and the cross-section (inset) of all samples. All these samples appeared to have a hexagonal shape nanorod with varied roughness ability. The pristine ZnO nanorod (ZP) claims a hexagonal shape ranging approximately 40 nm. At the same time, ZT1 and ZT5 exhibited rougher hexagonal surfaces with an elevated diameter owing to the construction of ZnTe and Te on the hybrid structures while satisfying the condition of being a nano-size material. Fig. 3d–i revealed the TEM images and the elemental mapping of the hybrid structure, reinforcing the nature of crystallinity and the element distribution in our nanohybrid structure. It was clear that the rod structure surface of ZnO was covered with ZnTe formation, indicating non-uniform ZnO-to-ZnTe conversion. However, the ZnTe cover layer was approximately 10 nanometers in ZT1. The interplanar distances corresponded to the ZnTe's (022) lattice plane and ZnO's (002) lattice plane, confirming the ZnTe formation. As shown in Fig. S1,† TEM analyses of ZT5 revealed the ZnTe layer and Te, agreeing with the information extracted from XRD and XPS measurements.

Fig. 4 illustrates the XPS information and characteristics of the deconvolution O 1s of the core level of the ZP, ZT1, and ZT5 samples under different light irradiation conditions to check the noticeable difference in chemical characterization between the samples. The deconvoluted peaks at binding energy 530 eV and 531 eV corresponded to lattice oxygen (Oi) and oxygen vacancy (Ov), respectively.[20] In the case of pristine ZnO, as shown in Fig. 4(a–c), the ratio of Ov/Oi remains negligibly unchanged under dark and blue cases, while under UV light illumination effect, the ratio of Ov increases which contributed to the sensing behavior of ZP under UV effect and agreed with the fact that ZnO only response to UV interaction.[25] It is evident that in the case of ZT1 under blue light irradiation, the Ov/Oi ratio increases significantly compared with the pristine ZP case, which contributes as one of the main proposed principles of the enhanced sensing behavior of ZT1. Oxygen vacancies can provide reacted sites for the adsorption of target gas molecules,

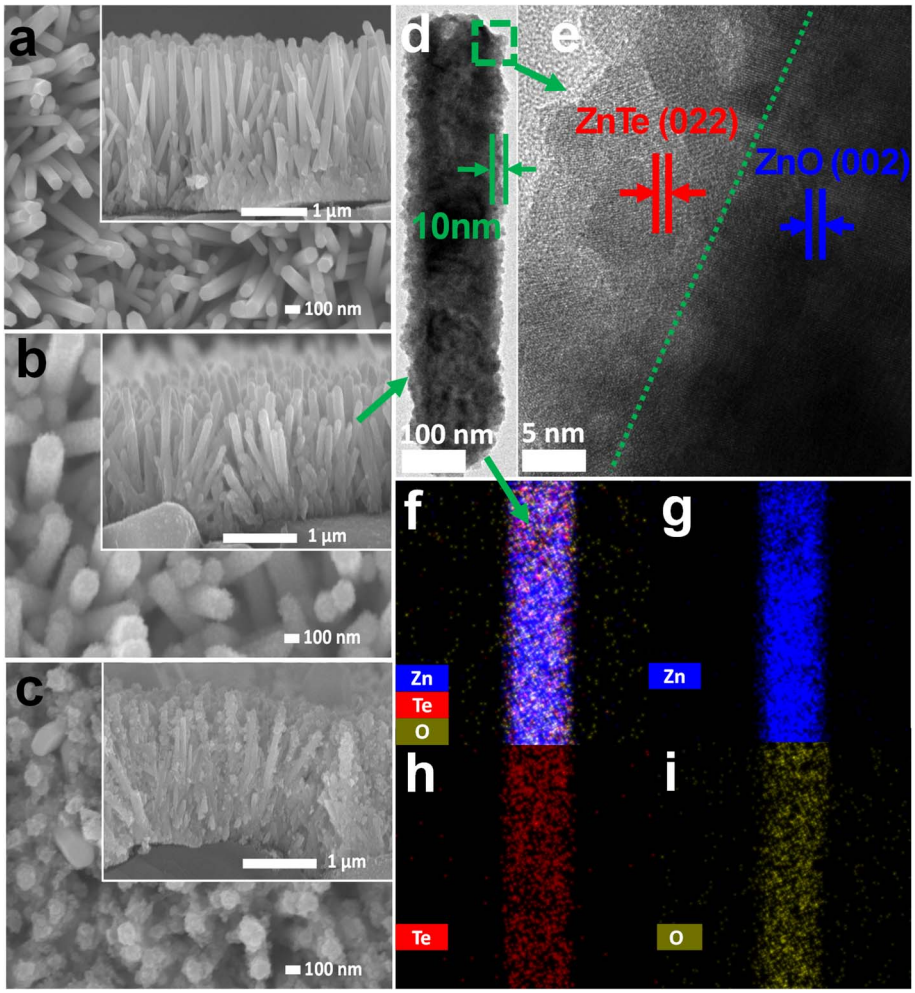

Fig. 3 Plan-view SEM illustration and cross-section images (inset) of (a) ZP, (b) ZT1, and (c) ZT5 samples. (d and e) TEM profiles of ZT1 and (f–i) elemental mapping images of ZT1.

Open Access Article. Published on 13 December 2024. Downloaded on 2/20/2026 8:43:14 PM.
This article is licensed under a Creative Commons Attribution-NonCommercial 3.0 Unported Licence.

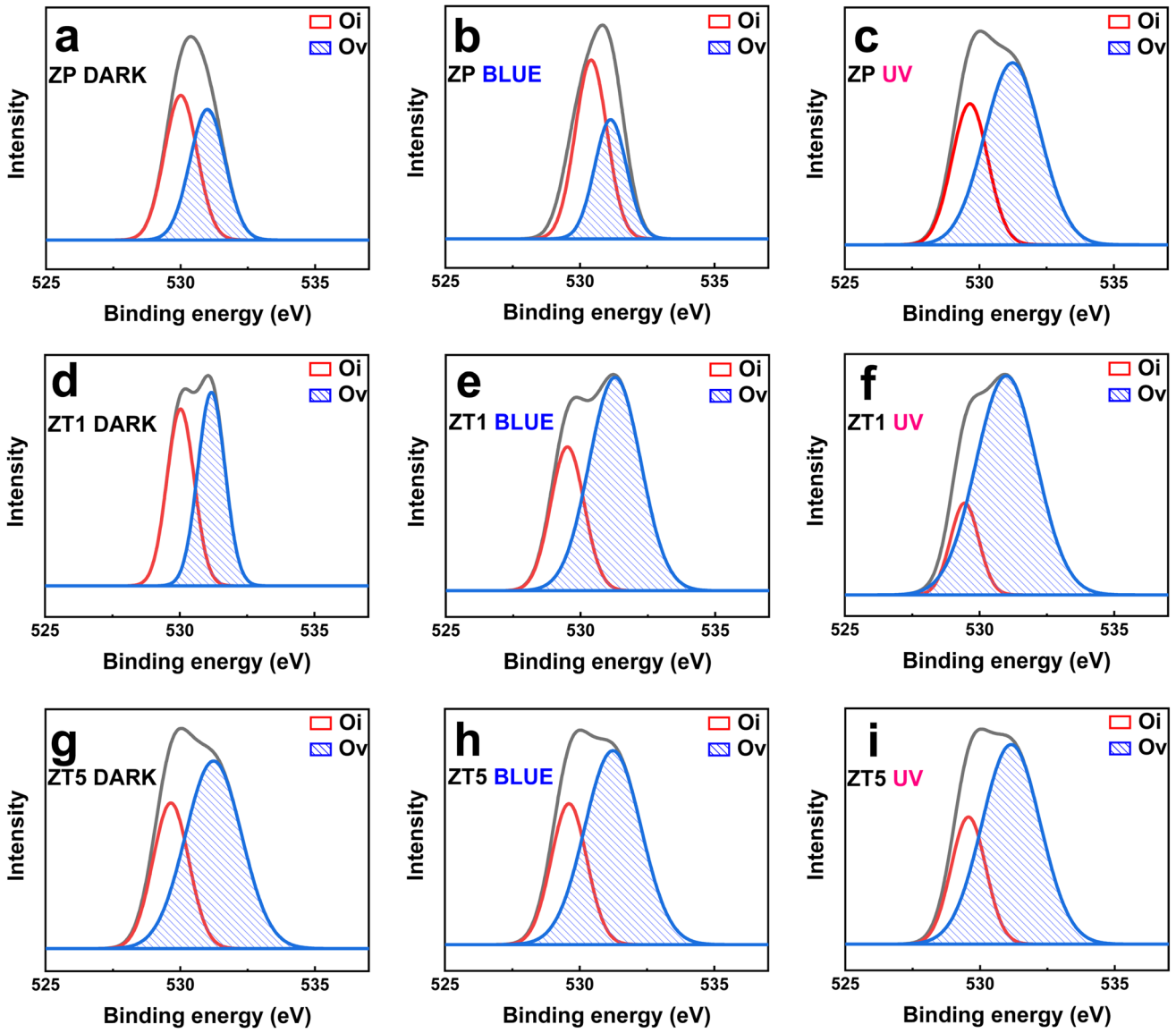

Fig. 4 Deconvoluted O 1s XPS core–level spectra of (a–c) ZP; (d–f) ZT1; (g–i) ZT5 under dark, blue, and UV light illumination effect.

modulate the amount of surface adsorbed oxygen, and alternatively, responsible for the gas detection principle.[20,38]

3.2 Gas response characteristics

Fig. 5a–i shows the changes in sensitivity measured toward 500 ppb NO_2 exposure of the labeled sensor devices at different light irradiation situations (under dark, blue, and UV, respectively) and provides some significant observations.

Firstly, the light effect enhancement toward samples is compared with dark conditions. At dark, the response of all 3 samples (ZP, ZT1, and ZT5) shows a slight change in resistance behaviors under NO_2 exposure at RT. Still, with the NO_2 off the line, all the sample curves show an incomplete recovery property. This confirms the normal behavior for most of the sensors when measuring gas at RT conditions, especially toward NO_2. The addition of light irradiation significantly enhances sensing behavior. Secondly, the hybrid structures demonstrate their superior performance over pristine ZnO. As we can see in Fig. 5b and c, the response behavior of ZP samples raised from 1.1 to 1.54 and 2.1 under blue and UV, respectively, and the recovery ability remained negligible at dark. Still, the same negligible recovery repeated after the NO_2 gas was off under the blue light effect but became more observable under UV light. However, the ZT1 and ZT5 reveal more noticeable results: the response of ZT1 increased from ~3 under dark to 13 (4 times) and 9 (3 times) under blue and UV, respectively, and secured faster response time and nearly back to base recovery ability as delivered in Fig. 5e and f while ZT5 witnesses a slight increase in response but maintains the improved response time and recovery time's behavior, which was demonstrated in Fig. 5h and i. As revealed above, the response of ZP, ZT1, and ZT5 under the blue light radiation is 1.54, 13, and 3, respectively, when compared to 2.1, 9.1, and 6.6 of the listed samples under UV

© 2024 The Author(s). Published by the Royal Society of Chemistry

Open Access Article. Published on 13 December 2024. Downloaded on 2/20/2026 8:43:14 PM.
This article is licensed under a Creative Commons Attribution-NonCommercial 3.0 Unported Licence.

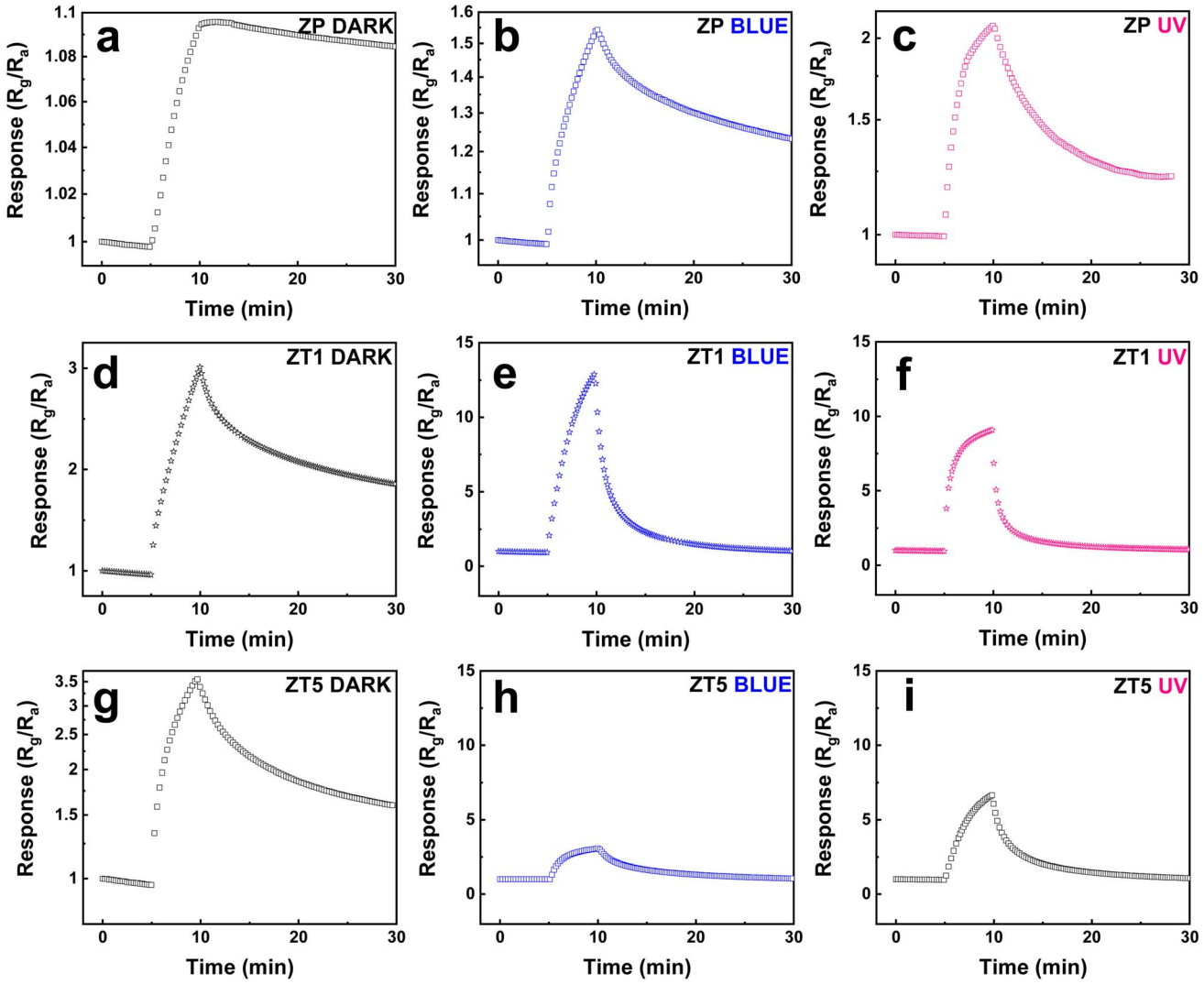

Fig. 5 Response curves to 500 ppb NO_2 of (a–c) ZP, (d–f) ZT1, (g–i) ZT5 under dark, blue, and UV irradiation sources.

light irradiation. This result illustrates that the response of ZT1 under the effect of blue light is better than UV, while ZP and ZT5 still obey the advantageous sensing behavior of UV. Thirdly, amongst measured hybrid structures (ZT1 and ZT5), when compared to ZnO/ZnTe/Te sample, the p–n junction ZnO/ZnTe under blue light irradiation shows the optimum performance while securing the highest response (R_g/R_a ~13), top 2 of response time (~44 s), and top 1 of recovery time (~20 min), which were shown in Fig. 6e and f *via* logarithmic changes of the signals.

The pristine ZnO exhibiting low resistance (~20 kΩ) under dark, as shown in Fig. 6d, has relatively massive intrinsic n-type defects, which cause a thin depletion depth. The cross-section of the nanorod was accordingly drawn in Fig. 7a, along with a large region of neutral inside. The depletion depth lately increased with a small gap while under the incoming NO_2 approach, which lately resulted in a low modulation of the depletion region depth, thus causing poor sensitivity. The additional light effect leads to the enhanced electron–hole-pairs (EHPs) in ZP with a slight rise in the sensing signal (Fig. 5b and c). In this situation, the size of the neutral core increased, but the depletion depth also increased due to the enhancement of photo-carriers to the NO_2 adsorption rate on the surface, thus resulting in a slight increase in response and recovery level. In the opposite direction, the enhanced sensitivity of the ZnO/ZnTe hybrid structure (ZT1) in the dark is attributed to the huge reduction of the conduction region in the ZnO nanorod originating from the formation of the p–n junction. This is proved by the hundred times increased resistance in the hybrid (~80 MΩ under blue and 120 kΩ under UV, as shown in Fig. 6d). Such significant behavior is sketched in Fig. 7a, which is performed by a far reduced area of the depletion region while R_g is defined as the adsorption rate of target gas molecules on the sensing material surface, which is also described as the rate of the supplied electron from the neutral core to the adjacent surface.[35–37] The NO_2 adsorption rate can be lower in ZnO/ZnTe hybrid compared to pristine ZnO, but it is available to contribute to a greater depletion depth modification due to an

Open Access Article. Published on 13 December 2024. Downloaded on 2/20/2026 8:43:14 PM.
This article is licensed under a Creative Commons Attribution-NonCommercial 3.0 Unported Licence.

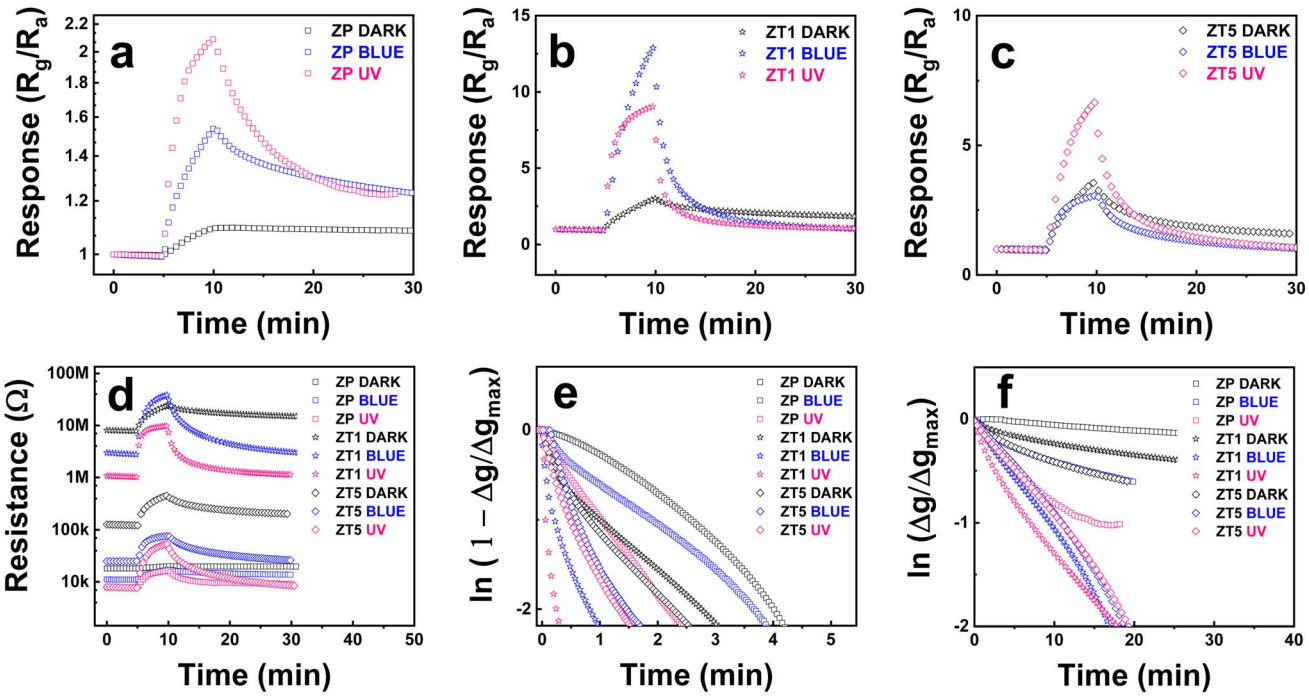

Fig. 6 (a–c) The response curves, (d) the resistance behaviors, the plots of (e) the response time, and (f) the recovery time of ZP, ZT1, and ZT5 toward 500 ppb NO_2 exposal at different light irradiation situations.

initial smaller neutral core value. As a result, a greater ratio of R_g/R_a leads to an increase in sensing response.

The plots of the response and recovery ability corresponded to exponential rise and decay behaviors of the response and recovery kinetics[39] were drawn above in Fig. 6e and f, confirming the prominence of light irradiation in sensing kinetics. From the graphs, the pristine ZnO indicates the prolonged response time and recovery time curve, which was due to the small ratio

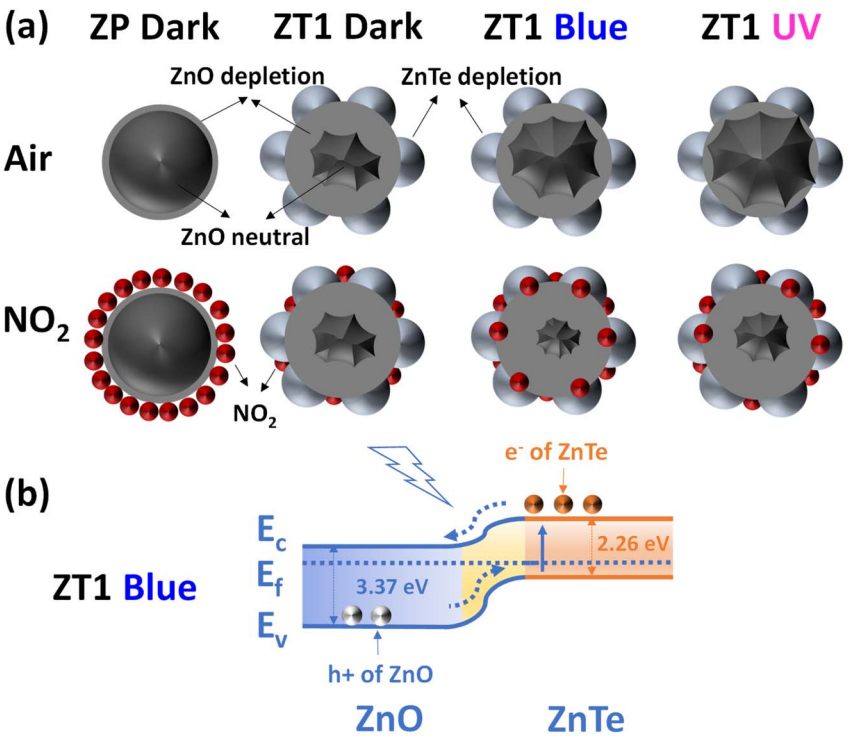

Fig. 7 (a) Mechanism scenario of ZP and ZT1 nanohybrid. (b) The energy band diagram of ZT1 under blue light irradiation.

© 2024 The Author(s). Published by the Royal Society of Chemistry

Open Access Article. Published on 13 December 2024. Downloaded on 2/20/2026 8:43:14 PM. This article is licensed under a Creative Commons Attribution-NonCommercial 3.0 Unported Licence.

of the number of favorable oxygen vacancies and the standard low dynamic adsorption rate of metal oxide material at room temperature. While the response time of ZP was huge under dark, the response time of ZT1 under blue and UV was 41 s and 12 s, and the response time of ZT5 under blue and UV was 89 s and 79 s, respectively. While the recovery time of ZP was undefinable under dark, the relevant recovery time of ZT1 under blue and UV is approximately 17 min, and the relevant recovery time of ZT5 under blue and UV is approximately 28 min. Generally, the adsorption and desorption processes are thermal activation; photon energy is supplied to help the gas target molecules overcome the adsorption energy barrier, and the adsorbed molecules overcome the desorption energy barrier. The pristine ZnO maintains the most extended response and recovery time, which was due to the small number of oxygen vacancies (or favorable adsorption areas). At the same time, ZT1 secures enhanced response and recovery behaviors possibly because of the higher number of available oxygen vacancies and the catalytic effects of ZnTe.[24] Meanwhile, the ZT5 structure contains both ZnTe and Te, and Te covers a particular surface area of the structure, and blocks or adsorbs the incoming gas molecules to the surface material, resulting in a lower response than the ZT1 hybrid nanostructure. Further response data are illustrated in Fig. S2.†

3.3 Proposed sensing mechanisms

The proposed sensing mechanism is described based on the theory of electron depletion layer, due to the n-type sensing behavior of all the measured sensors. At room temperature, in air, the following reactions can happen:[40,41]

$$O_2\,(g) \rightarrow O_2\,(ads) \quad (1)$$

$$O_2\,(ads) + e^- \rightarrow O_2^-\,(ads)\ (\text{with } T < 100\ ^\circ\text{C}) \quad (2)$$

$$NO_2\,(g) + e^- \rightarrow NO_2^-\,(ads) \quad (3)$$

$$NO_2\,(ads) + O_2^-\,(ads) + 2e^- \rightarrow NO_2^-\,(ads) + 2O^-\,(ads) \quad (4)$$

$$NO_2^-\,(ads) + 2O^-\,(ads) + e^- \rightarrow NO_2\,(gas) + 2O^{2-}\,(ads) \quad (5)$$

The dominant oxygen species at RT is O_2^-, and when NO_2 gas with high electron affinity (~2.28 eV) was introduced into the chamber, the adsorbed NO_2^- molecules could receive more electrons. As a result of the electron deduction from the surface of the materials, the electron depletion layer increases, which leads to the resistance increase, thus the enhancement in sensing behavior. As shown in Fig. 6a, the response behavior of ZP is negligible and the recovery time is undefinable. In contrast, ZP under light effect shows enhanced response (with UV claiming the highest value) and response time but the recovery behavior still meets obstacles at room temperature. Following by Fig. 6b, ZT1 under blue light irradiation claims the optimum performance in most of the aspects: response, response time, and recovery time, which affirm the opinion that ZnTe addition provides good enhancement and bonus stack in sensitivity ability. Finally, Fig. 6c provides ZT5 sensing behavior, the response time is acceptably accelerated, and the recovery behavior is back to near the initial base, but the sensitivity is reduced significantly, which was due to the blocking barrier of Te. Along with the modification of oxygen lattice – oxygen vacancies we mentioned in Section 3.1, all the observations above confirm the good catalytic effect of ZnTe (ZT1) in comparison to pristine ZnO (ZP) or ZnO/ZnTe/Te (ZT5) composition.

In addition, light irradiation generates structural defects on the surface of the sensing materials, which leads to the facilitation of oxygen vacancy adsorption, and promotes the reaction of adsorbed oxygen and electrons, affecting the charge carrier transportation in materials. The shining effect of light on the ZT1 structure reduces the resistance of ZT1 but is still higher than the pristine ZnO (ZP) in the dark. Thus, the depletion depth of ZT1 blue and UV is higher than ZP dark and smaller than ZT1 dark, which was illustrated in Fig. 7a. The light effect narrows the depletion region with the addition of electron carriers while increasing the electron supply rate to the surface which leads to the NO_2 adsorption's enhancement. Therefore, the charge difference between dark and light cases is huge, and the enhanced sensitivity of ZT1 under blue and UV can be explained by the conduction model for nanostructured sensors.

ZT1 in the dark exhibits a greatly expanded depletion layer region due to the p–n junction formation but negligibly expanded under NO_2 exposure. ZT1 under light irradiation with narrowed depletion depth region due to photo-carriers existence, but the NO_2 adsorption rate increases, leading to a higher depletion depth region modulation. ZT1 under blue irradiation and UV irradiation differed from each other since ZnTe and Te have mostly adsorbed UV, the depletion layer region narrowed not as high as in blue's case, and the NO_2 adsorption rate is not as strong as blue irradiation conditions. The band diagram of the ZT1 samples was illustrated in Fig. 7b, in which, under the appropriate provided energy of light effect (the energy of blue is 2.7 eV, and UV is 3.4 eV, respectively), the electron in the valence band of ZnTe get exited and move to the conduction band, which lately has higher mobility and freedom to join the ionosorption and other reaction occurred at the surface of the hybrid structure. In addition, the electron move to the ZnO area and contribute huge effort as the transducer role in the hybrid receptor/transducer strategy, which was mentioned before in our previous research.[36,37,42] In our work, blue light with a photon energy of 2.7 eV has better sensing improvement toward nanohybrid structure than UV light with a photon energy of 3.4 eV. To explain that blue light rarely stimulates the status change of electrons between the valence and conduction bands in ZP (as shown in Fig. 6d with the negligible shift of base resistance of ZP under blue light in comparison to the base resistance of ZP under dark). In contrast, UV light provides significant change which is relatively sensible due to the appropriate wavelength of UV. With the appearance of the nanohybrids ZT1 and ZT5, the change was significantly enhanced, as described in Fig. 6. Due to the modification of the narrow bandgap ZnTe, the formation of p–n junction nanohybrid exceptionally exhibits greater enhanced light absorption, which created widely a good chance for blue irradiation to

Open Access Article. Published on 13 December 2024. Downloaded on 2/20/2026 8:43:14 PM.
This article is licensed under a Creative Commons Attribution-NonCommercial 3.0 Unported Licence.

Table 1 Comparison between this work and others. The terms NRs, NPs, and NSs refer to Nanorods, nanoparticles, and nanosheets, respectively

Material	Response	Concentration (ppm)	λ (nm)	Temperature (°C)	Ref.
ZnO–rGO (NRs)	2.83	10	365	175	15
ZnO–SnO_2 (NRs–NPs)	2.5	0.2	380	RT	44
ZnO–Au (NSs)	0.623	1–5	365	RT	45
ZnO–Zn_2SnO_4 (NRs)	0.807	1–5	365	RT	46
ZnO–Ag (NPs)	1.545	0.5	470	RT	47
ZnO–In_2O_3 (microtube)	18	5	460	RT	48
ZnO–ZnTe (NRs)	**15**	**0.5**	**460**	**RT**	**This work**

stimulate the degree of freedom of electron, leading to an enhancement in electron carrier charge rate and results in the sensitivity improvement. With the same intensity as light sources, UV has higher energy but provides fewer photons than blue light, which is beneficial for blue light to create more exited electrons for enlisted in the gas sensing process. Lately, in the case of ZT5, the blocking barrier surrounding Te limits the incoming light irradiation source to significantly affect sensing materials such as ZT1.

Considering another aspect of the available proposed explanation, the absorption coefficient of a material can be calculated as below:

$$\alpha(\lambda) = \frac{4\pi\kappa}{\lambda} \quad (6)$$

where κ is the imaginary part of the complex refractive index or so-called extinction coefficient, and λ is the wavelength of the incident light. The refractive index data of ZnTe, Te, and ZnO are taken from the reference. As illustrated in Fig. S3,† ZnO has average small absorption coefficients at different wavelengths of light sources, while ZnTe showed the highest energy absorption efficiency at shorter wavelengths and gradually decreased as wavelengths increased. In addition, Te always maintained good energy absorption efficiency at various types of light incoming sources. Therefore, this result significantly explained the phenomenon of ZnTe/ZnO at blue light has a smaller absorption ability than ZnO/ZnTe/Te, which led to more space of p–n heterojunction to modify the depletion layer and the charge carrier incomes, which resulted in an enhanced response characteristic. It also pulled out another explanation of why the ZnO/ZnTe nanohybrid structure secured better sensing performance at blue light than UV light since UV has been absorbed at the finest and left small space to interfere with enhancing the gas detection.

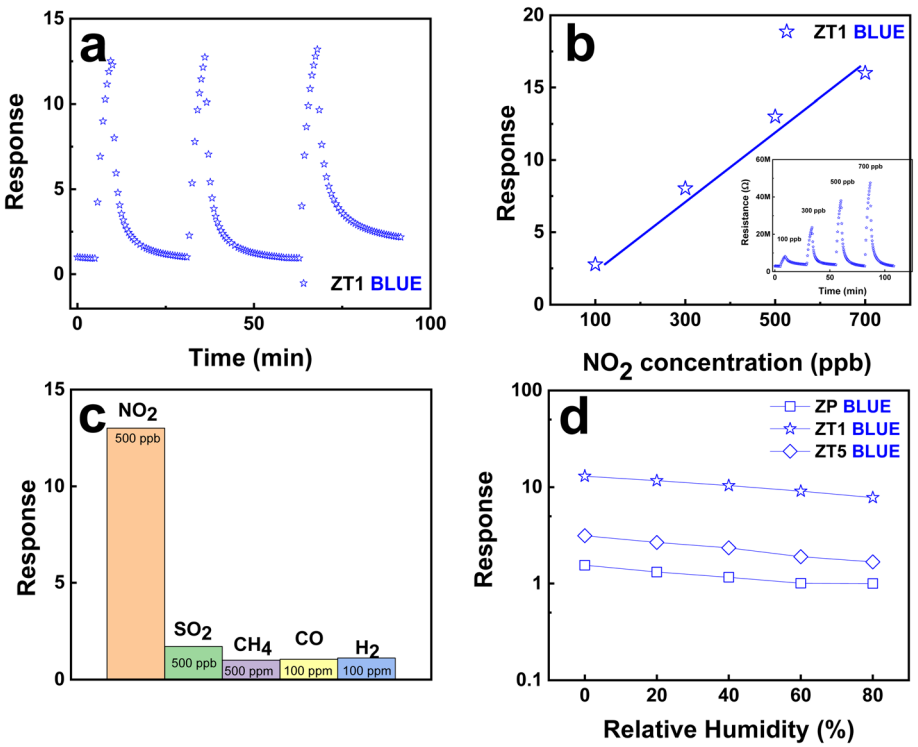

Fig. 8 (a) The repeatability of ZT1 upon exposure to 500 ppb NO_2 under blue light irradiation at RT. (b) The sensitivity linearity behavior of ZT1 upon exposure to different NO_2 exposure concentrations under blue light irradiation at RT (with the inset illustrating the corresponding resistance behaviors). (c) The response curves of ZT1 measured at RT toward 500 ppb NO_2 at dark/under blue irradiation effect with different humidity values. (d) Selectivity of our NO_2 gas sensors compared to other gases.

© 2024 The Author(s). Published by the Royal Society of Chemistry

Open Access Article. Published on 13 December 2024. Downloaded on 2/20/2026 8:43:14 PM. This article is licensed under a Creative Commons Attribution-NonCommercial 3.0 Unported Licence.

Another proposal is based on the findings illustrated in Fig. 2 of the ref. 43, the attraction force between two objects will be enhanced if the material is altered from dielectric metallic. Notice that ZnO has a bandgap of ~3.37 eV while ZnTe secures a 2.26 eV bandgap, which means ZnTe has better "metallic" properties. This suggests that ZnTe layer addition can increase the attractiveness of force with NO_2 gas and enhance the interaction between NO_2 and electrons.

The sensing performance of our hybrid structures shows significant improvements when compared with other works, as shown in Table 1.

3.4 Humidity effect and repeatability properties

Fig. 8a confirms the good repeatability behavior of ZT1 during the sensing process and the potential for a further stable manufacturing process. ZT1, under blue light irradiation at RT, claims the linear dependence on the NO_2 concentration as shown in Fig. 8b with the raw resistance data attached in the inset. Thus, the lowest NO_2 gas concentration ZT1 can reach is 100 ppb, which further claims the advantage of this hybrid structure in the development era of small-scale gas detectors. ZT1 also shows excellent selectivity among different gases of H_2, CO, CH_4, and SO_2 as shown in Fig. 8c. The selectivity is significantly high with respect to the examined gases by showing a relatively small response to 0.5–500 ppm concentrations. Fig. 8d summarizes the effect of humidity on the gas-sensing behavior of ZT1 under the blue light impact at RT toward 500 ppb NO_2. The observation shows that the response decreases with increasing the relative humidity in the ambient environment. This phenomenon is due to the reduction of adsorption sites, occupied by the abundant water molecules. Therefore, fewer approaching NO_2 molecules are adsorbed on the surface of the sensing material, leading to a smaller response. The irradiated gas sensors show a slower reduced response speed than the pristine ZnO, which could be because NO_2 molecules prefer to be chemisorbed on the defective hybrid surface, compared with H_2O molecules. However, the observation is not well-obtained and the sensing behavior of our hybrid structure under humidity and light effect requires further study. The ZT1 sensor secures good reproducibility through ten consecutive days of repeating the same sensing measurements as shown in Fig. S4.†

4. Conclusions and future perspectives

ZnO/ZnTe nanohybrid structures were successfully synthesized by the facile double hydrothermal method and revealed linearity enhancement of NO_2 sensing properties under light irradiation effect at RT. The greater sensing performance amongst the hybrids is the ZT1 sensor under blue light irradiation, including its good selectivity and well-repeated sensing behavior. A systematic exploration of the linearity sensing enhancement mechanism and sensing phenomena within the nanohybrid structures was conducted to understand this study comprehensively. The ZnTe addition increases the available adsorption sites for the gas molecules with the increased oxygen vacancies while creating the p–n junction's formation, the modified depletion layers, associating with the photo carrier effect, which significantly enhances nanohybrid adsorption site density and good sensing. The nanohybrid between metal oxide semiconductors and ZnTe can be a good candidate for developing oxidizing gas sensors at RT under light effect. Further additional studies on diversified semiconductor sources should be conducted in further research.

Data availability

The data supporting this article have been included as part of the ESI.†

Conflicts of interest

There are no conflicts to declare.

Acknowledgements

This research is funded by Phenikaa University under grant number PU2023-1-A-03. This work was supported by Phenikaa University and Chungnam National University.

References

1 J. Xuan, G. Zhao, M. Sun, F. Jia, X. Wang, T. Zhou, G. Yin and B. Liu, *RSC Adv.*, 2020, **10**, 39786–39807.
2 N. M. Elsayed, *Toxicology*, 1994, **89**, 161–174.
3 J. A. Bernstein, N. Alexis, C. Barnes, I. L. Bernstein, A. Nel, D. Peden, D. Diaz-Sanchez, S. M. Tarlo and P. B. Williams, *J. Allergy Clin. Immunol.*, 2004, **114**, 1116–1123.
4 Y. Jian, W. Hu, Z. Zhao, P. Cheng, H. Haick, M. Yao and W. Wu, *Nanomicro Lett.*, 2020, **12**, 1–43.
5 S.-J. Choi and I.-D. Kim, *Electron. Mater. Lett.*, 2018, **14**, 221–260.
6 A. Mirzaei, J.-H. Kim, H. W. Kim and S. S. Kim, *J. Mater. Chem. C*, 2018, **6**, 4342–4370.
7 A. Mirzaei, J.-H. Lee, S. M. Majhi, M. Weber, M. Bechelany, H. W. Kim and S. S. Kim, *J. Appl. Phys.*, 2019, **126**, 241102.
8 T. Hyodo and Y. Shimizu, *Anal. Sci.*, 2020, **36**, 401–411.
9 C.-J. Chang, C.-Y. Lin, J.-K. Chen and M.-H. Hsu, *Ceram. Int.*, 2014, **40**, 10867–10875.
10 S. T. Shishiyanu, T. S. Shishiyanu and O. I. Lupan, *Sens. Actuators, B*, 2005, **107**, 379–386.
11 M. Bai, M. Chen, X. Li and Q. Wang, *Sens. Actuators, B*, 2022, **373**, 132738.
12 P. Cao, Y. Cai, D. Pawar, S. T. Navale, C. N. Rao, S. Han, W. Xu, M. Fang, X. Liu and Y. Zeng, *Chem. Eng. J.*, 2020, **401**, 125491.
13 X. Chen, Y. Shen, P. Zhou, X. Zhong, G. Li, C. Han, D. Wei and S. Li, *Sens. Actuators, B*, 2019, **289**, 160–168.
14 P. Rai, Y.-S. Kim, H.-M. Song, M.-K. Song and Y.-T. Yu, *Sens. Actuators, B*, 2012, **165**, 133–142.
15 S. K. Shaikh, V. V Ganbavle, S. I. Inamdar and K. Y. Rajpure, *RSC Adv.*, 2016, **6**, 25641–25650.

© 2024 The Author(s). Published by the Royal Society of Chemistry

Open Access Article. Published on 13 December 2024. Downloaded on 2/20/2026 8:43:14 PM. This article is licensed under a Creative Commons Attribution-NonCommercial 3.0 Unported Licence.

16 M. S. Choi, M. Y. Kim, A. Mirzaei, H.-S. Kim, S. Kim, S.-H. Baek, D. W. Chun, C. Jin and K. H. Lee, *Appl. Surf. Sci.*, 2021, **568**, 150910.
17 Y. Kang, F. Yu, L. Zhang, W. Wang, L. Chen and Y. Li, *Solid State Ionics*, 2021, **360**, 115544.
18 V. Paolucci, J. De Santis, L. Lozzi, M. Rigon, A. Martucci and C. Cantalini, *Ceram. Int.*, 2021, **47**, 25017–25028.
19 S. M. Mali, P. P. Chavan, Y. H. Navale, V. B. Patil and B. R. Sathe, *RSC Adv.*, 2018, **8**, 11177–11185.
20 J. H. Bang, Y. J. Kwon, J.-H. Lee, A. Mirzaei, H. Y. Lee, H. Choi, S. S. Kim, Y. K. Jeong and H. W. Kim, *J. Hazard. Mater.*, 2021, **416**, 125841.
21 T. Wang, J. Chen, J. Chen, X. Yao, G. Chen, Z. Jiao, J.-T. Zhao, S. Cheng, X.-C. Yang and Q. Li, *Appl. Surf. Sci.*, 2023, **641**, 158551.
22 Q. Zhang, G. Xie, M. Duan, Y. Liu, Y. Cai, M. Xu, K. Zhao, H. Tai, Y. Jiang and Y. Su, *ACS Appl. Nano Mater.*, 2023, **6**, 17445–17456.
23 T. Mahalingam, V. Dhanasekaran, K. Sundaram, A. Kathalingam and J.-K. Rhee, *Ionics*, 2012, **18**, 299–306.
24 M. F. Ehsan, M. N. Ashiq and T. He, *RSC Adv.*, 2015, **5**, 6186–6194.
25 M. Iqbal, Y. Wang, H. Hu, M. He, A. H. Shah, P. Li, L. Lin, A. R. Woldu and T. He, *Electrochim. Acta*, 2018, **272**, 203–211.
26 N. M. Hieu, T. T. Hien, N. D. Chinh, N. D. Quang, N. M. Hung, C. Van Phuoc, S.-M. Lee, J.-R. Jeong, C. Kim and D. Kim, *Mater. Des.*, 2020, **191**, 108628.
27 A.-M. Panaitescu and V.-A. Antohe, *Coatings*, 2023, **13**, 208.
28 J. He, C. Niu, C. Yang, J. Wang and X. Su, *RSC Adv.*, 2014, **4**, 60253–60259.
29 J.-H. Kim, A. Mirzaei, H. Woo Kim, P. Wu and S. S. Kim, *Sens. Actuators, B*, 2019, **293**, 210–223.
30 S. O. Aisida, R. M. Obodo, M. Arshad, I. Mahmood, I. Ahmad, F. I. Ezema, T. Zhao and M. Malik, *Nucl. Instrum. Methods Phys. Res., Sect. B*, 2019, **458**, 61–71.
31 J. Hu, J. Zhang, X. Liu, H. Zhang, X.-X. Xue and Y. Zhang, *Appl. Surf. Sci.*, 2023, **623**, 157093.
32 J. Chang, C. Qin, W. Guo, L. Zhu, Y. Zhang, Y. Wang and J. Cao, *Sens. Actuators, B*, 2023, **385**, 133633.
33 N. M. Hieu, C. Van Phuoc, C. V. Anh, N. M. Hung, A. D. Phan, N. D. Chinh, S. Majumder, P. T. Huy, J.-R. Jeong and J. Nah, *Ceram. Int.*, 2023, **49**, 16944–16950.
34 N. M. Hieu, C. Van Phuoc, N. M. Hung, C. V. Anh, A. D. Phan, J. Nah, J.-R. Jeong, P. T. Huy and D. Kim, *Sens. Actuators, A*, 2023, **351**, 114141.
35 N. D. Chinh, T. T. Hien, L. Do Van, N. M. Hieu, N. D. Quang, S.-M. Lee, C. Kim and D. Kim, *Sens. Actuators, B*, 2019, **281**, 262–272.
36 N. M. Hung, N. M. Hieu, N. D. Chinh, T. T. Hien, N. D. Quang, S. Majumder, G. Choi, C. Kim and D. Kim, *Sens. Actuators, B*, 2020, **313**, 128001.
37 N. M. Hieu, C. Van Phuoc, T. T. Hien, N. D. Chinh, N. D. Quang, C. Kim, J.-R. Jeong and D. Kim, *Sensors*, 2019, **19**, 3915.
38 M. Al-Hashem, S. Akbar and P. Morris, *Sens. Actuators, B*, 2019, **301**, 126845.
39 N. M. Vuong, D. Kim and H. Kim, *Sens. Actuators, B*, 2015, **220**, 932–941.
40 S. Drewniak, Ł. Drewniak and T. Pustelny, *Sensors*, 2022, **22**, 5316.
41 F. Zhang, Q. Lin, F. Han, Z. Wang, B. Tian, L. Zhao, T. Dong and Z. Jiang, *Microsyst. Nanoeng.*, 2022, **8**, 40.
42 N. D. Chinh, Y. Haneul, N. M. Hieu, N. M. Hung, N. D. Quang, C. Kim and D. Kim, *J. Colloid Interface Sci.*, 2021, **584**, 582–591.
43 A. D. Phan and N. A. Viet, *Phys. Rev. A:At., Mol., Opt. Phys.*, 2011, **84**, 062503.
44 G. Lu, J. Xu, J. Sun, Y. Yu, Y. Zhang and F. Liu, *Sens. Actuators, B*, 2012, **162**, 82–88.
45 Y. Mun, S. Park, S. An, C. Lee and H. W. Kim, *Ceram. Int.*, 2013, **39**, 8615–8622.
46 S. Park, S. An, H. Ko, C. Jin and C. Lee, *Ceram. Int.*, 2013, **39**, 3539–3545.
47 Q. Zhang, G. Xie, M. Xu, Y. Su, H. Tai, H. Du and Y. Jiang, *Sens. Actuators, B*, 2018, **259**, 269–281.
48 Y. Li, X. Wei, Q. Liu, D. Zang and R. You, *ACS Sens.*, 2024, **9**, 3741–3753.

© 2024 The Author(s). Published by the Royal Society of Chemistry